Research Square

Preprints are preliminary reports that have not undergone peer review.
They should not be considered conclusive, used to inform clinical practice,
or referenced by the media as validated information.

Stepwise formation of authigenic clay from biogenic silica: are elemental and alkalinity sinks still coupled during reverse weathering?

Simin Zhao

siminzhao21@gmail.com

Georgia Institute of Technology

Hailiang Dong

China University of Geosciences (Beijing)

Christopher Reinhard

Georgia Institute of Technology

Wenqian Xu

Argonne National Laboratory

Yuanzhi Tang

Georgia Institute of Technology

Article

Keywords: revere weathering, authigenic clay, silicate weathering, enhanced weathering, carbon cycle, alkalinity sink, elemental sink, decoupling

Posted Date: November 17th, 2026

DOI: https://doi.org/10.21203/rs.3.rs-11436975/v1

License: This work is licensed under a Creative Commons Attribution 4.0 International License.
Read Full License

Additional Declarations: No competing interests reported.

Abstract

The formation of authigenic clays in marine sediments, termed “reverse weathering”, is important in regulating marine elemental sinks, seawater chemistry, and CO2 dynamics in the modern ocean and throughout Earth’s history. Classically, sequestration of Si, cation, and alkalinity has been considered concurrent and treated as a coupled process, allowing reverse-weathering rates and associated elemental sinks to be estimated from one another reverse-weathering signatures. Yet, the relationship among the intertwined elemental sinks remains poorly resolved. In this study we show authigenic Fe-clay formation from biogenic silica proceeds via a stepwise process involving rapid initial precipitation of amorphous Al-Si precursors within hours, followed by slower Fe^{2+}-driven transformation and cation incorporation to form Fe^{2+}-smectite in 2–6 months. The timescale and partitioning of Fe^{2+} and other cations during the transformation are strongly regulated by Fe^{2+} concentration. Our results suggest that Si burial, cation sequestration, and alkalinity removal during reverse weathering are stepwise and kinetically partitioned rather than synchronously fixed, challenging long-standing formulations employing bulk coupled equilibrium sinks with concurrent elemental sequestration used to infer global elemental budgets. This work provides a step towards establishing a more robust framework for estimating reverse weathering–associated global elemental and alkalinity sinks in response to changing inputs from terrestrial weathering and anthropogenically-modulated enhanced rock weathering.

Introduction

The sources and sinks of elemental fluxes in the ocean shape seawater composition[1,2], element bioavailability, and bioproductivity[3–6].Terrestrial weathering of silicate rocks consumes CO_2, leading to the input of alkalinity (HCO_3^-) and influxes of elements (e.g., Si, cations, nutrients) to the ocean, regulating atmospheric CO_2 dynamics and global climate over geological time scales[7–9]. In contrast to forward silicate weathering, reverse weathering in marine environments[10,11] is generally expressed as:

$$bSiO_2 + Al(OH)_4^- + (Fe^{2+3+}, Mg^{2+}, K^+, Li^+) + HCO_3^- \rightarrow \text{aluminosilicates} + CO_2 + H_2O\uparrow .$$

This process converts HCO_3^- to CO_2, buffers ocean alkalinity,[10–13] and transforms biogenic silica ($bSiO_2$) to cation-rich authigenic aluminosilicate clay minerals in ambient marine environments.

The broader significance of reverse weathering for ocean chemistry and climate were only begun to be considered due to the overlooked prolonged time scale of 10^3–10^6 years and low reaction rates at ambient temperature[14]. The advancement of understanding of reverse weathering’s timescale has improved from seminal field incubations and sediment isotope studies[11,15–19] with observed reverse weathering reactions at time scales on the order of years to months to the most recent studies that further demonstrated this processes to be extremely robust and responsive – on timescales of days to weeks.[20,21]. In parallel, the mechanistic understanding of reverse weathering has identified dissolution and reprecipitation mechanism[15,22] with sediment reducing redox conditions and inputs of Al and Fe

from lithogenic fluxes being conducive to form authentic clay from direct and indirect evidence by field incubations and sediment isotopic signatures[11,15–17,23–26]. These studies have led to an increasingly recognized dynamic nature and importance of reverse weathering in controlling atmospheric CO_2 dynamics[11,12,26–29], oceanic budgets of Si, Fe, K, and alkalinity (HCO_3^-), and sea water chemistry[30,31], with consequent effects on primary production and global climate. For example, reverse weathering has recently been recognized as second largest Si output in the oceanic Si budget[29] (4.5 to 4.9 Tmol Si/year), as a significant sink of porewater dissolved iron in both modern and ancient sediments[4,27], and as a dynamic contributor to marine alkalinity budgets across geologic time[7,12,28,32]. The advances may also inform the fate and durability of alkalinity generated by enhanced rock weathering for climate mitigation which is expected to introduce increased scale of lithogenic inputs to marine environment with response from reverse weathering [21,33].

Despite the improved constraints on the timescale and geochemical triggers, the pathways governing the coupled elemental sequestration and partitioning of elements remain unresolved for reverse weathering. Nonetheless, current frameworks for reverse weathering as an elemental and alkalinity sink have been built based on an overall dissolution-reprecipitation process which is applied essentially as an equilibrium sink for Si, cations (Mg, Al, Fe, K, Li, etc.), and alkalinity when reverse weathering occurs. Estimates of cation sinks associated with reverse weathering have primarily been derived from analyses of cation precipitation in authigenic phases combined with sedimentation rate and porewater cation profiles coupled with modeling[4,11,16,21,27,30,34–36]. In addition, several studies has also applied authigenic clay cation (e.g., K)/Si stoichiometric ratios to infer the scale of cation fluxes from Si measurements in the field[11,16]. Associated Si flux rates, phase transformation, and Si sinks have been estimated by field Si alkaline extraction, pore water profile measurement, Si or Si coupled with cation isotopic signatures, and sediment diagenetic modeling applied to infer the magnitude of authigenic clay formation and rates of reverse weathering from Si sources (e.g., biogenic silica, lithogenic Si) in modern marine environments[11,15,16,18,19,21,24,37]. Estimation of alkalinity and carbon cycling by reverse weathering has been constructed through assumed coupling of Si and HCO_3^- via stoichiometric relationships in authigenic clay[7,12,28] and multi-element stoichiometic coupling[38]. For example, previous studies generally apply the alkalinity (Alk) to silica (Si) ratio (Alk:Si) associated with authigenic clay to infer alkalinity removal by reverse weathering with Si uptake both in modern and ancient environments[7,12,28]. However, these approaches assume direct precipitation and instantaneous, synchronous elemental incorporation.

Elucidating the interplay, partitioning, and elemental coupling pathways of dissolved species in resulting authigenic phases during reverse weathering remains a critical challenge to resolve before these coupled mechanisms can be robustly applied to quantitatively estimate elemental sinks and carbon cycling. In this study, we investigate the reverse weathering reaction coupling mechanism during Fe-clay formation from diatom $bSiO_2$ with intermittent Al inputs and varying dissolved Fe^{2+} concentration under simulated anoxic marine sedimentary conditions. With this experimental setting, we directly elucidated

the coupled and decoupled elemental sequestrations during authigenic phase formation. The findings have important implications in building a robust framework for the fate and estimation of alkalinity and elemental sinks in response to inputs from silicate weathering, biogeochemical cycling, and anthropogenically- modulated enhanced rock weathering.

Results

Discrete partitioning of Si, Al, and Fe in solution phase evolution

Solution phase monitoring during the first 60 days showed only the 1000 μM Fe^{2+} treatment (Fe1000) had a significant decrease in Fe^{2+} concentration (Fig. 1A), consuming ~ 40 μM Fe^{2+}. Lower Fe^{2+} treatments from 0 to 500 μM (Fe0–Fe500) showed no significant changes in dissolved Fe^{2+} (Fig. 1B). In contrast, rapid decreases in dissolved Si (by ~ 50 μM) and Al (almost all of the spiked 40 μM) were observed for all treatments during the first two days (Fig. 1C, D), likely caused by the coprecipitation of Si and Al. A small amount of Si (~ 20 μM) continued to decrease in the Fe1000 treatment from day 2 to 60, likely caused by the precipitation with Fe^{2+} (Fig. 1A) At day 60, a second spike of dissolved Al (40 μM) was added, and similar patterns of decreasing Si (by ~ 20–30 μM) and Al (by ~ 40 μM) were observed for all Fe^{2+} treatments (Fig. 1C and D). From day 60 to 180, Fe^{2+} in the Fe1000 treatment continued to decrease, consuming an additional ~ 173 μM of Fe^{2+}. Interestingly, although the Fe500 and Fe300 treatments did not show significant changes in Fe^{2+} concentration during day 0–60, both showed gradual decreases in Fe^{2+} during day 60–180 (~ 97 μM for Fe500 and ~ 30 μM for Fe300). No Fe^{2+} concentration change was observed for Fe100 treatment.

Kinetically partitioned Fe-smectite formation governed by Fe

Formation of Si-Al precursor or Fe-smectite within 2 months at varied Fe^{2+} conc.

The solid products from all treatments harvested on day 60 (before the second Al spike) and at day 180 showed corresponding discrete mineral phase formation in line with solution-phase observations (hereafter, we refer to these solid samples with their Fe treatment and reaction time, e.g., Fe1000-day180). At day 60, consistent with the evolution of dissolved Fe^{2+}, the formation of an Fe-clay phase was observed in Fe1000 treatment (Fig. 2 and Figure S1) but not in other treatments (Figure S2). Synchrotron X-ray diffraction (XRD) analysis of the reacted solids showed the formation of a new peak at 1.564 Å in Fe1000-day60 (Fig. 2A), a characteristic peak of d_{060} for Fe^{2+}-smectite[39,40]. High-resolution transmission electron microscopy (HRTEM) (Fig. 2B) and scanning electron microscopy (SEM) (Figure S1) analyses of this new phase showed a distinct curved, flaky morphology growing on bSiO_2. Further HRTEM analysis revealed a turbostratic layered structure with d-spacings of 10 Å (d_{001}) and 3.1 Å (d_{003}) (Fig. 2C), which are characteristic of the large interlayer spacing of smectite[39,41,42]. Selected area

electron diffraction (SAED) analysis identified the new phase to be crystalline with d-spacings of 1.60 Å (d_{006}) and 3.1 Å (d_{003}), typical of smectite[39–41,43]. Energy dispersive spectroscopy (EDS) showed a Fe/Mg-bearing aluminosilicate composition but concentrations of cations like K and Ca were below detection. These combined morphological, lattice fringe, and compositional characteristics indicate the formation of Fe-smectite in Fe1000-day60[39–42], in line with authigenic green clay reported in marine environments [27,44]. Contrary to the Fe1000 sample but consistent with the evolution of dissolved Si and Al, all other Fe^{2+} treatments only showed the formation of an Al-Si amorphous phase under SEM-EDS (Figure S2).

Crystalline Fe-smectite formation within 6 months at high Fe^{2+} conc.

SEM, TEM, and synchrotron analysis all showed the formation of Fe-smectite (Fig. 3) at the end of 180 days. In sample Fe1000-day180, a new curved flaky phase grew extensively on bSiO_2 (Fig. 3, A1–A4). SAED of this new phase showed a crystalline structure with d-spacings of 5.00 Å (d_{002}), 2.70 Å (d_{200}), 1.60 Å (d_{006}), and 1.45 Å (d_{330}), typical of smectite[39–41,43]. EDS revealed a Fe-Mg-bearing aluminosilicate composition with small amounts of K and Ca (Fig. 3A) which were likely incorporated as interlayer cations[40]. HRTEM analysis further confirmed a turbostratic layered structure with a d-spacing of 10 Å (d_{001}) (Fig. 3), consistent the d-spacings of the Fe-smectite observed in Fe1000-day60 (Fig. 2C). SEM examination showed extensive production of this Fe-smectite phase (Fig. 3) as compared to Fe1000-day60 (Fig. 2B, S3A). The structure and Fe oxidation state of the new phases were confirmed by synchrotron XRD and Fe K-edge X-ray absorption spectroscopy (XAS) (Fig. 3B and Figure S3). The characteristic peaks of Fe-smectite is consistent with that observed in the well-crystalline Fe-rich trioctahedral smectite synthesized by Chemtob et al. using a hydrothermal method[39]. A comparison of Fe-smectite formed on day 60 and day 180 indicates increased crystallinity and Fe content in the Fe-smectite structure (Fig. 3B and 2B, Supplementary Material S1). To our knowledge, this is the first comprehensive identification and confirmation of Fe-bearing authigenic clay by synchrotron techniques.

(Trans)formation to Fe-smectite after 6 months with lower Fe^{2+} conc.

In Fe500-day180, a curved, flaky phase similar to 10 Å Fe-smectite and containing Mg, K, and Ca was observed (Fig. 4, A-C), but less as abundant compared to Fe1000-day180 (Fig. 3A). An amorphous Al-Si bearing phase with less-defined morphology (granule-shaped) was also observed (Fig. 4, B–C) and confirmed to be amorphous by HRTEM (Figure S4). To differentiate this phase from the curved, flaky Fe-smectite phase, we refer to them as amorphous Al-Si granules and Fe-smectite flakes, respectively. Similar amorphous Al-Si granules were also observed in the Fe500 to Fe0 treatments on day 60 (Supplementary Material; Figure S2). Collectively, based on the observed chemical composition, morphology, and close proximity, we hypothesize that the Fe-smectite flakes are a later stage transformation product from the amorphous Al-Si granules. The observation is consistent in sample Fe300-day180, where similar curved 10 Å Fe-smectite flakes containing low levels of Ca were observed but at even smaller amounts (Fig. 4, D1–F), with d-spacings typical of smectite observed by SAED.

Similar to sample Fe500-day180, amorphous Al-Si granules were more prominent containing only small amounts of Fe (Fig. 4B) and the Fe-smectite flakes appeared to grow from these amorphous granules (Fig. 4B and C). Collectively, a comparison of samples Fe1000, Fe500, and Fe300 showed a decreasing extent of Fe-smectite formation from Fe1000 to Fe300. Consistent with aqueous phase observation, no Fe-smectite formation was observed in the Fe100 and Fe0 samples, and only amorphous Al-Si rich granules were observed throughout the experimental course (Figure S5) by SEM, supported by synchrotron XRD confirming the formation of the new phase only in Fe1000, Fe500, and Fe300 after day 180 (Fig. 3B, Supplementary Material Text S1). Comparison of the harvested solids show green clay formation in the Fe1000, Fe500, and Fe300 treatment groups while not in the Fe100, and Fe0 treatment groups (Fig. 5). The change of dark green in Fe1000 treatment to light green in Fe300 treatment also suggests the decreasing formation extent of green Fe-smectite.

Discussion

Authigenic Fe-clay formation is a rapid, stepwise process

Here, we show rapid formation of an Fe^{2+}-smectite clay phase in the presence of dissolved Al and Fe^{2+} within 2–6 months under conditions applicable to sediment reverse weathering. Our incubations across a gradient of dissolved Fe^{2+} concentrations (300–1000 μM) and sporadic Al inputs common in marine sedimentary settings indicate that reverse weathering can occur rapidly and robustly and suggest that ambient Fe-clay formation in marine sediments may far more dynamic than previously recognized. To our knowledge this is the first comprehensive and dynamic examination and report of the Fe^{2+}-smectite clay formation with elemental partitioning unraveled under reverse weathering conditions. In addition to Fe-smectite, a variety of authigenic phases (e.g., Fe-muscovite, illite, greenalite, berthierine, chamosite, glauconite)[4,11,22,42,45,46] have been reported in modern marine diagenetic settings and in the rock record from marine environments[11,12,42,47], though most of these have not been directly confirmed as products of reverse weathering. Nonetheless, smectite is one of the dominant clay phases in marine sediments[48,49], and ubiquitously referred to as green clay in field observations[27,44]. Smectite and the above-mentioned authigenic phases are interchangeable and can transform into one another during diagenesis[50]. For example, muscovite can transform to smectite and illite, and smectite can transform to illite to form mixed-layer phases including glauconite.[40,51,52] Taken together, the reported Fe^{2+}-smectite phase here represents a major authigenic phase which can further transform into other clay phases commonly reported in marine sediments and sedimentary rocks.

The formation mechanism of Fe-smectite is demonstrated here to be a stepwise, progressive process (Fig. 6B), providing an in-depth mechanistic understanding of elemental partitioning and coupling compared to the conventional dissolution-reprecipitation framework (Fig. 6A). This novel pathway involves dissolution of $bSiO_2$ (Step 1), precipitation of dissolved Si into an amorphous Al-Si precursor phase triggered by dissolved Al (Step 2), followed by the incorporation of Fe^{2+} and alteration of the amorphous Al-Si phase to crystalline Fe^{2+}-smectite (Step 3) with concurrent cation (Mg, K, and Ca)

uptake. The partitioning of Mg, K, and Ca is in line with the understanding that Mg can substitute Fe^{2+}/Al^{3+} at the tetrahedral sites in Fe-aluminosilicate clay phases with incorporation of K^+ and Ca^{2+} as interlayer charge-balancing ions[27,40]. The extent and crystallinity of Fe^{2+}-smectite product in Step 3 is positively correlated to Fe^{2+} concentration and reaction time. Step 3 is also observed to be a slower process compared to Steps 1 and 2, and thus likely is the rate-controlling step for the overall reverse weathering reaction. We discuss these specific steps and their limitations below.

For Step 2, the formation of the amorphous Al-Si phase might be intermittent and triggered by sporadic local inputs of dissolved Al, such as dissolution of sedimentary Al-bearing minerals[17]. For Step 3, the transformation of the Al-Si phase to Fe-smectite is also constrained: higher Fe^{2+} concentration can led to higher reaction rate for solution phase and higher transformation extent and crystallinity of the Fe-smectite as a result of nucleation and aging, while longer reaction time despite at lower Fe^{2+} concentration (compare Fe300 and Fe500 at day 60 and day 180) can also led to higher transformation extent and formation of the Fe-smectite. The concentrations of Fe^{2+} in our experiments are common in marine environments (e.g., deltaic sediments, mangrove forests, saltmarsh sediments, and estuaries[11,22,45,53–55]) and can result in gradients in Fe-smectite formation kinetics and extents. Previous work speculated the participation of Fe^{2+} in authigenic clay formation during reverse weathering in Amazon deltaic sediments [22] and deduced diagenesis of Fe in reducing deltaic environments[26]. Our results demonstrate the governing role played by Fe^{2+} in reverse weathering kinetics and provide the first direct evidence that higher Fe^{2+} concentration (under reducing condition, ~ 500–1000 μM) can trigger more rapid and extensive Fe^{2+}-smectite formation in a given timeframe. In marine sediments, sporadic high input of Fe^{2+} resulted from anoxia and reactive continental runoff materials may trigger more rapid authigenic Fe-smectite formation. This is in line with the observed rapid authigenic clay formation in response to local coastal El Nino at Peruvian margin that brought increased reactive continental run-off [20].

Implications for alkalinity sink and global elemental fluxes

Reverse weathering-induced authigenic clay formation has been proposed to be an oceanic sink of Si, cations (e.g., Fe, K, Ca, and Mg), and alkalinity (HCO_3^-) from terrestrial weathering inputs in both the modern and ancient ocean[4,27,29,31,32,46,56,57]. By coupling HCO_3^- consumption to CO_2 release, reverse weathering is of profound importance for regulating atmospheric CO_2 dynamics and Earth's climate[7–9,12,28]. An increasing number of studies have incorporated reverse weathering in global carbon budget and both in the modern and throughout Earth history [7,28]. A similar growth of attention in reverse weathering's modulating effect in Si removal [6,29] for balancing oceanic Si budgets as well as the sinks for other important elements including Fe, K, Ca, and Mg[4,27,31,32,56,57]. Estimation of individual sinks is usually intertwined i.e.; one built upon others. Current estimation sinks fluxes relied on field measurements of porewater fluxes, wet chemical sediment extractions, isotopic fractionation of

sediment phases, extrapolated reaction rates (e.g., based on isotopic signals), and model-based calculations [17–19,24,28,38] (Table S1). Recent studies have applied cosmogenic Si, stable Si, Be, Li, and K isotopes as proxies to fingerprint Si uptake by authigenic clay formation in reverse weathering[18,19,23,24,26,36,38,58] (Table S1). Based on the conventional dissolution-reprecipitation mechanism[15,22], studies have considered the final precipitated products as a quasi-instantaneous bulk sink for all elemental fluxes (Fig. 6A). Within this conventional framework, the sinks of Si, alkalinity, and other cations are usually jointly considered and flux estimates are built upon each other when exploring the contribution of modern reverse weathering to elemental sinks[7,12]. For example, a consumption ratio between alkalinity and Si (Alk:Si), scaled to cation/Si ratios, is assumed in order to translate the modern annual Si flux (extracted by Si isotopic and Si wet chemistry extraction methods[16,18,19]) to a flux of carbon through R[7]. Models attempting to isolate the role of reverse weathering as a CO_2 regulator thus extrapolate reverse weathering rates[28] based on Si isotope results or field measurements of Si fluxes[16,19,24,38]. Estimated fluxes of cations (K and Li) have also been scaled based on cation to Si ratios (e.g., K/Si and Li/Si) in authigenic products[11,19].

However, such estimation assumes synchronous sinks for individual elemental fluxes involved in the re-precipitation process. In contrast, our results demonstrate that authigenic formation is a stepwise process and that the sequestration of Si, cations, and alkalinity might be decoupled: the sinks of Si, Al, Fe^{2+} and other cations, and HCO_3^- are associated with different products at different steps (Al-Si amorphous phase or final Fe-clays). Thus, these individual sinks should not be assumed to occur synchronously, but rather in discrete stages constrained by time frame and reaction products (Fig. 6B). The precipitated Al-Si rich and cation-poor amorphous precursor phase in Step 2 serves as a sink for Si and Al. However, because this step/product does not consume alkalinity, it does not contribute to CO_2 release[7,12]. The consumption of alkalinity only occurs in Step 3, during which the incorporation of Fe^{2+} and other cations (K, Ca, and Mg) transforms the amorphous Si-Al precursor phase to an Fe-clay phase. In modern environmental settings, these steps and related timescales will be controlled by local sediment conditions. For example, in deltaic or benthic environments, the dissolution of Al-containing mineral phases[22,59] can trigger rapid passage through the Step 2 reaction, as observed by previously reported inverse relationship between dissolved Si and Al porewater concentrations in marine sediments within hours,[60,61]. The precursor phases may have long-formed before the inputs of cation-rich triggers transformation. The supply of Fe^{2+} from reductive dissolution of Fe-minerals for Step 3 could be constrained by seasonal conditions and terrestrial lithogenic inputs such as delta front summer hypoxia[25,62], seasonal fluctuations of benthic sediment oxygen penetration depth[62], or seasonal weather events such as coastal El Nino[20].. Consequently, field measurements of reverse weathering rates using Si-based methods, while capturing the Si sink, may not accurately reflect consumption of cations and alkalinity. In parallel, rates of reverse weathering extrapolated from cation-based isotopic tools[23,26,36,38] may not always scale directly to Si fluxes.

Taken together, we recommend revisiting the definition, contribution, and impacts of reverse weathering to the individual elemental sinks of Si, HCO_3^-, and cations, in order to further quantify individual elemental fluxes globally. We postulate that the sink discrepancy due to such stepwise Fe-clay authigenesis is constrained by time scale of months to years based on the observed transformation time frames in our experiment. Thus, the stepwise clay authigenesis would likely not affect field measurements and estimations based on aged, well-crystalline ancient sediment samples which had gone through mature transformation over Earth's history; instead, it may primarily affect estimates of modern reverse weathering sinks derived from measurements over relatively short timescales, an issue that may become increasingly important with the large-scale deployment of enhanced rock weathering (ERW) implemented for climate mitigation. Given that common feedstocks of ERW such as olivine and basalt are usually Fe-Mg rich[33,63], the dissolution inputs may create conducive conditions for cation-rich authigenic clay formation with alkalinity release. Accounting for these will therefore be important to optimize deployment approach and refining Measurement, Reporting, and Verification to accurately capture the fate and effectiveness of ERW.

As a result, the estimation of elemental sinks from Si, cation isotopic approaches (e.g., Li, Be, Ca, Mg, K) and field porewater profile measurements need to be deconvoluted in inferring reverse weathering rates and corresponding elemental budgets. With respect to the Si sink, we suggest field Si measurements and Si isotopic signatures applied to estimate modern Si sinks are less likely to be impacted by the dynamics of stepwise Fe-clay formation, for reasons discussed above. However, the rate and magnitude of Si sequestration could not be applied to equivalently infer to rates of authigenic clay formation and reverse weathering. Similarly, the reverse weathering rate extrapolated from other isotopic approaches (e.g., Li, Be, Ca, Mg, K) would not be identically translated to Si sequestration rates and budgets. Additionally, we postulate that authigenic phases may not necessarily form on $bSiO_2$ substrates as observed in this study, but possibly on other non-biological substrates if readily available during burial in sediments[58] or the Si-Al precursors more dynamically. Sediment phase selection for field Si measurements should thus be considered accordingly. With respect to estimating alkalinity and cation sinks by applying extrapolated Si- measurements, Alk/Si ratio, and cation/Si ratios, we suggest extra sediment treatment procedures for field Si measurements may be needed to rule out the effects of intermediate Al-Si amorphous phases. Lastly, sediment diagenesis models and Earth system modeling attempt to extrapolate reverse weathering rates and evaluate the impact of reverse weathering on global CO_2 dynamics should consider stepwise clay authigenesis and the time scale of relevant phase formation/transformation in authigenic phase selection and model design.

Materials and Methods

Materials and reagents

Diatom frustules from the marine species *Thalassiosira pseudonana* was used as the $bSiO_2$ source. The diatom biomass was obtained from Reed Mariculture Inc. and repeatedly rinsed with deionized (DI)

water (18 MΩ cm) to remove residual growth media until the conductivity reaches < 10 μS cm^{-1}. The material was then freeze-dried, gently ground, and placed in a glass petri dish for organic matter removal by low temperature plasma ashing (Plasma-Thermal RIE) following our previous procedure[64]. The structure of the obtained $bSiO_2$ material was characterized by XRD (PANalytical Empyrean, Cu Kα source) and showed an amorphous structure (Figure S6). Surface area of the $bSiO_2$ material is 53 m^2/g as reported in our previous work[64].

All experiments were conducted inside a Coy anaerobic glove box (95/5 N_2/H_2) using anoxic DI water. Anoxic DI water was prepared by sterilizing DI water under UV light for an hour, followed by boiling on a hot plate, then allowed to naturally cool down while purged by ultra-high purity N_2 gas. After cooling, the DI water bottle was capped and brought into the glove box. The dissolved oxygen level of the DI water was periodically tested using the Rhodazine D™ Method test kit (CHEMetrics K-7599, 5 ppb detection limit of dissolved oxygen). Anoxic stock solutions of $FeCl_2$, $AlCl_3$, DSi (as Na_2SiO_3), and artificial seawater (ASW, pH 7.5, buffered by 15 mM HEPES)[65] were prepared inside the glove box using the anoxic DI water. The ASW was prepared at pH 7.5, representing the general pH of delta, continental shelf, and river fan sediment pore waters [11,66].

Experimental setup

Biogenic silica incubation experiments were conducted in replicates in borosilicate serum bottles under simulated sedimentary conditions with a range of initial Fe^{2+} concentration and dissolved Al spiked at different time points. Plasma-cleaned organic-removed $bSiO_2$ solids (0.1 g/L) were suspended in anoxic ASW and allowed to dissolve until the DSi reached ~ 380–400 μM (Figure S7), representing lower than medium DSi concentration in marine sediment pore water concentration [12,22]. Dissolved Fe^{2+} (as $FeCl_2$) was added to the reaction bottle at a range of representative pore water concentrations, including no Fe^{2+} (control), low Fe^{2+} at 100 μM (e.g., Mississippi and Amazon delta[53,67]), intermediate Fe^{2+} at 300 μM (e.g., coastal marine sediments[55]), and high Fe^{2+} at 500 and 1000 μM (e.g., continental shelf of the northern Gulf of Mexico and Congo River fan sediments[66]). Dissolved Al (40 μM) was added in spikes both at the beginning of the experiment and day 60. Although dissolved Al concentration in marine sediment is generally very low (nM)[60] due to the low solubility of Al hydroxide phases at marine sedimentary pH, local transient higher concentrations (μM) of Al flux from Al mineral dissolution is possible [21,68]. The serum bottles were constantly agitated on a shaker table (120 rpm).

Characterization of solution and solid phases

The time-course evolution of solution and solid phases was monitored during the incubation. At each sampling point, a small aliquot of the reaction suspension was collected, syringe filtered (0.1 μm), and immediately acidified using a small amount of concentrated trace-metal grade HNO_3. Dissolved Fe^{2+} and

DSi in the filtrate were quantified using the ferrozine method[69] and molybdenum blue method[70], respectively. Dissolved Al was measured by inductively coupled plasma–mass spectrometer (ICP-MS). At given time points, solid phases were harvested using 0.1 μm filter, air dried in a gloved box, and characterized for composition, morphology, and structure using SEM-EDS, HRTEM, synchrotron XRD, and synchrotron XAS, as detailed below.

For ICP-MS analysis, solution samples were diluted using DI water and trace-metal grade HNO_3. Indium (20 ppb) was added to each sample as an internal standard to monitor instrument drift. Standard solutions with a range of dissolved Al concentration (1–200 ppb) were prepared and measured every 20–30 samples to ensure measurement accuracy.

SEM-EDS analysis was conducted on a Hitachi SU-8230 SEM equipped with an Oxford EDS detector with a spatial resolution of 0.8 nm at 15 KeV and 1.1 nm at 1 KeV. SEM images were obtained at a low accelerating voltage (5 KeV) and a short working distance (8 mm). EDS spectra were obtained at a high accelerating voltage (15 KeV) and longer working distance (15 mm).

Based on SEM-EDS results, the neoformed mineral phases were further examined by HRTEM. A small quantity of reacted solids was dispersed in ethanol and the suspension was placed onto a lacey carbon coated copper grid and air dried. HRTEM and selected area electron diffraction (SAED) analyses were conducted on a FEI Tecnai F30 TEM equipped with thermally assisted field emission gun and operated at 300 KeV.

The structure of the neoformed phases was also analyzed using synchrotron XRD and Fe K-edge XAS at Beamlines 17-BM (λ = 0.45191Å) and 12-BM-B, at the Advanced Photon Source (APS) at Argonne National Laboratory, Lemont, IL, USA. Samples were loaded to epoxy sealed Kapton capillary tubes and heat sealed in a polyethylene bag inside a glove box to maintain anoxic conditions[39]. For Fe K-edge XAS, both XANES and EXAFS data were collected. Energy calibration used Fe foil. XAS data analysis was performed using the software Athena[71]. Multiple scans (4–6) were collected for each sample, averaged, and normalized.

Declarations

Competing interests

The authors declare no competing interests.

Data and materials availability

All data needed to evaluate the conclusions in the paper are present in the paper and/or the Supplementary Materials which includes a PDF file for supplementary text and figures and an Excel file

for compiled solution phase data.

Author Contribution

S.Z. and Y.T. conceived the study. S.Z. designed and conducted the experiments with assistance from W.X. Y.T. supervised the project and obtained funding support. S.Z. analyzed data and wrote the manuscript. S.Z., H.D., C. R., and Y.T. revised the manuscript. All authors edited the manuscript.

Acknowledgement

This work is funded by the National Science Foundation grants OCE-1559087 (YT). We thank beamline scientists at Beamlines 12-BM and 17-BM at Advanced Photon source (APS). Use of APS is supported by the US Department of Energy, Office of Sciences, Office of Basic Energy Sciences, under Contract No DE-AC02-06CH11357.

Data Availability

All data needed to evaluate the conclusions in the paper are present in the paper and/or the Supplementary Materials which includes a PDF file for supplementary text and figures, and an Excel file for compiled solution phase data.

References

1. Holland, H. D. Sea level, sediments and the composition of seawater. *American Journal of Science* 305, 220, doi:10.2475/ajs.305.3.220 (2005).
2. Jeandel, C. & Oelkers, E. H. The influence of terrigenous particulate material dissolution on ocean chemistry and global element cycles. *Chemical Geology* 395, 50–66, doi:https://doi.org/10.1016/j.chemgeo.2014.12.001 (2015).
3. Armbrust, E. V. The life of diatoms in the world's oceans. *Nature* 459, 185–192, doi:10.1038/nature08057 (2009).
4. Baldermann, A., Warr, L. N., Letofsky-Papst, I. & Mavromatis, V. Substantial iron sequestration during green-clay authigenesis in modern deep-sea sediments. *Nature Geoscience* 8, 885–889, doi:10.1038/ngeo2542 (2015).
5. Shoenfelt, E. M. *et al.* High particulate iron(II) content in glacially sourced dusts enhances productivity of a model diatom. *Science advances* 3, e1700314-e1700314, doi:10.1126/sciadv.1700314 (2017).
6. Treguer, P. J. & De La Rocha, C. L. in *Annual Review of Marine Science, Vol 5* Vol. 5 *Annual Review of Marine Science* (eds C. A. Carlson & S. J. Giovannoni) 477–501 (Annual Reviews, 2013).

7. Isson, T. T. *et al.* Evolution of the Global Carbon Cycle and Climate Regulation on Earth. *Global Biogeochemical Cycles* 34, e2018GB006061, doi:https://doi.org/10.1029/2018GB006061 (2020).
8. Kump, L. R., Brantley, S. L. & Arthur, M. A. Chemical Weathering, Atmospheric CO2, and Climate. *Annual Review of Earth and Planetary Sciences* 28, 611–667, doi:10.1146/annurev.earth.28.1.611 (2000).
9. Struyf, E., Smis, A., Van Damme, S., Meire, P. & Conley, D. J. The Global Biogeochemical Silicon Cycle. *Silicon* 1, 207–213, doi:10.1007/s12633-010-9035-x (2009).
10. Mackenzie, F. T. & Garrels, R. M. Chemical mass balance between rivers and oceans. *American Journal of Science* 264, 507–525 (1966).
11. Michalopoulos, P. & Aller, R. C. Rapid clay mineral formation in Amazon delta sediments: reverse weathering and oceanic elemental cycles. *Science*, 614–614 (1995).
12. Isson, T. T. & Planavsky, N. J. Reverse weathering as a long-term stabilizer of marine pH and planetary climate. *Nature* 560, 471–475, doi:10.1038/s41586-018-0408-4 (2018).
13. Mackenzie, F. T. & Garrels, R. M. Silica-bicarbonate balance in the ocean and early diagenesis. *Journal of Sedimentary Research* 36, 1075–1084, doi:10.1306/74D715FF-2B21-11D7-8648000102C1865D (1966).
14. Odin, G. S. & Fröhlich, F. Chapter C3 Glaucony from the Kerguelen Plateau (Southern Indian Ocean). *Developments in Sedimentology* 45, 277–294, doi:http://dx.doi.org/10.1016/S0070-4571(08)70068-2 (1988).
15. Loucaides, S. *et al.* Seawater-mediated interactions between diatomaceous silica and terrigenous sediments: Results from long-term incubation experiments. *Chemical Geology* 270, 68–79, doi:10.1016/j.chemgeo.2009.11.006 (2010).
16. Michalopoulos, P. & Aller, R. C. Early diagenesis of biogenic silica in the Amazon delta: Alteration, authigenic clay formation, and storage. *Geochimica Et Cosmochimica Acta* 68, 1061–1085, doi:10.1016/j.gca.2003.07.018 (2004).
17. Michalopoulos, P., Aller, R. C. & Reeder, R. J. Conversion of diatoms to clays during early diagenesis in tropical, continental shelf muds. *Geology* 28, 1095–1098, doi:10.1130/0091-7613(2000)28%3C1095:codtcd%3E2.0.co;2 (2000).
18. Rahman, S., Aller, R. C. & Cochran, J. K. Cosmogenic 32Si as a tracer of biogenic silica burial and diagenesis: Major deltaic sinks in the silica cycle. *Geophysical Research Letters* 43, 7124–7132, doi:https://doi.org/10.1002/2016GL069929 (2016).
19. Rahman, S., Aller, R. C. & Cochran, J. K. The Missing Silica Sink: Revisiting the Marine Sedimentary Si Cycle Using Cosmogenic 32Si. *Global Biogeochemical Cycles* 31, 1559–1578, doi:10.1002/2017GB005746 (2017).
20. Geilert, S. *et al.* Coastal El Niño triggers rapid marine silicate alteration on the seafloor. *Nature Communications* 14, 1676, doi:10.1038/s41467-023-37186-5 (2023).
21. Zhao, S. *et al.* Rapid transformation of biogenic silica to authigenic clay: Mechanisms and geochemical constraints. *Science Advances* 11, eadt3374, doi:10.1126/sciadv.adt3374.

22. Aller, R. C. in *Treatise on Geochemistry, Second Edition* Vol. 8 (eds Holland H.D. & Turekian K.K.) 293–334 (Elsevier, 2014).
23. Bernhardt, A. *et al.* 10Be/9Be Ratios Reveal Marine Authigenic Clay Formation. *Geophysical Research Letters* 47, e2019GL086061, doi:https://doi.org/10.1029/2019GL086061 (2020).
24. Ehlert, C. *et al.* Stable silicon isotope signatures of marine pore waters - Biogenic opal dissolution versus authigenic clay mineral formation. *Geochimica Et Cosmochimica Acta* 191, 102–117, doi:10.1016/j.gca.2016.07.022 (2016).
25. Presti, M. & Michalopoulos, P. Estimating the contribution of the authigenic mineral component to the long-term reactive silica accumulation on the western shelf of the Mississippi River Delta. *Continental Shelf Research* 28, 823–838, doi:10.1016/j.csr.2007.12.015 (2008).
26. Zhang, X., Gaillardet, J., Barrier, L. & Bouchez, J. Li and Si isotopes reveal authigenic clay formation in a palaeo-delta. *Earth and Planetary Science Letters* 578, 117339, doi:https://doi.org/10.1016/j.epsl.2021.117339 (2022).
27. Baldermann, A. *et al.* Impact of green clay authigenesis on element sequestration in marine settings. *Nature Communications* 13, 1527, doi:10.1038/s41467-022-29223-6 (2022).
28. Krissansen-Totton, J. & Catling, D. C. A coupled carbon-silicon cycle model over Earth history: Reverse weathering as a possible explanation of a warm mid-Proterozoic climate. *Earth and Planetary Science Letters* 537, 116181, doi:https://doi.org/10.1016/j.epsl.2020.116181 (2020).
29. Tréguer, P. J. *et al.* Reviews and syntheses: The biogeochemical cycle of silicon in the modern ocean. *Biogeosciences* 18, 1269–1289, doi:10.5194/bg-18-1269-2021 (2021).
30. Santiago Ramos, D. P., Morgan, L. E., Lloyd, N. S. & Higgins, J. A. Reverse weathering in marine sediments and the geochemical cycle of potassium in seawater: Insights from the K isotopic composition (41K/39K) of deep-sea pore-fluids. *Geochimica et Cosmochimica Acta* 236, 99–120, doi:https://doi.org/10.1016/j.gca.2018.02.035 (2018).
31. Sun, X., Higgins, J. & Turchyn, A. V. Diffusive cation fluxes in deep-sea sediments and insight into the global geochemical cycles of calcium, magnesium, sodium and potassium. *Marine Geology* 373, 64–77, doi:https://doi.org/10.1016/j.margeo.2015.12.011 (2016).
32. Dunlea, A. G., Murray, R. W., Santiago Ramos, D. P. & Higgins, J. A. Cenozoic global cooling and increased seawater Mg/Ca via reduced reverse weathering. *Nature Communications* 8, 844, doi:10.1038/s41467-017-00853-5 (2017).
33. Baldermann, A. *et al.* Exploring reverse silicate weathering across geological time: a review. *Clay Minerals* 60, 1–27, doi:10.1180/clm.2024.27 (2025).
34. Harder, H. Synthesis of Iron Layer Silicate Minerals under Natural Conditions. *Clays and Clay Minerals* 26, 65–72, doi:10.1346/CCMN.1978.0260108 (1978).
35. Higgins, J. A. & Schrag, D. P. Constraining magnesium cycling in marine sediments using magnesium isotopes. *Geochimica et Cosmochimica Acta* 74, 5039–5053, doi:https://doi.org/10.1016/j.gca.2010.05.019 (2010).

36. Li, W. *et al.* Potassium isotope signatures in modern marine sediments: Insights into early diagenesis. *Earth and Planetary Science Letters* 599, 117849, doi:https://doi.org/10.1016/j.epsl.2022.117849 (2022).
37. Baronas, J. J., Hammond, D. E., Rouxel, O. J. & Monteverde, D. R. A First Look at Dissolved Ge Isotopes in Marine Sediments. *Frontiers in Earth Science* Volume 7–2019, doi:10.3389/feart.2019.00162 (2019).
38. Wallmann, K. *et al.* Silicate weathering in anoxic marine sediments. *Geochimica et Cosmochimica Acta* 72, 2895–2918, doi:https://doi.org/10.1016/j.gca.2008.03.026 (2008).
39. Chemtob, S. M., Nickerson, R. D., Morris, R. V., Agresti, D. G. & Catalano, J. G. Synthesis and structural characterization of ferrous trioctahedral smectites: Implications for clay mineral genesis and detectability on Mars. *Journal of Geophysical Research: Planets* 120, 1119–1140, doi:https://doi.org/10.1002/2014JE004763 (2015).
40. Moore, D. M. *X-ray diffraction and the identification and analysis of clay minerals / Duane M. Moore and Robert C. Reynolds, Jr*. (Oxford University Press, 1989).
41. Badaut, D. & Risacher, F. Authigenic smectite on diatom frustules in Bolivian saline lakes. *Geochimica et Cosmochimica Acta* 47, 363–375, doi:https://doi.org/10.1016/0016-7037(83)90259-4 (1983).
42. Velde, B. in *Treatise on Geochemistry* (eds Heinrich D. Holland & Karl K. Turekian) 309–324 (Pergamon, 2003).
43. Manceau, A., Chateigner, D. & Gates, W. P. Polarized EXAFS, distance-valence least-squares modeling (DVLS), and quantitative texture analysis approaches to the structural refinement of Garfield nontronite. *Physics and Chemistry of Minerals* 25, 347–365, doi:10.1007/s002690050125 (1998).
44. Geilert, S., Frick, D. A., Abbott, A. N. & Löhr, S. C. Marine clay maturation induces systematic silicon isotope decrease in authigenic clays and pore fluids. *Communications Earth & Environment* 5, 573, doi:10.1038/s43247-024-01746-4 (2024).
45. Cuadros, J. *et al.* The mangrove reactor: Fast clay transformation and potassium sink. *Applied Clay Science* 140, 50–58, doi:https://doi.org/10.1016/j.clay.2017.01.022 (2017).
46. Tosca, N. J., Guggenheim, S. & Pufahl, P. K. An authigenic origin for Precambrian greenalite: Implications for iron formation and the chemistry of ancient seawater. *GSA Bulletin* 128, 511–530, doi:10.1130/B31339.1 (2016).
47. Hazen, R. M. *et al.* Clay mineral evolution. *American Mineralogist* 98, 2007–2029, doi:10.2138/am.2013.4425 (2013).
48. Cole, T. G. & Shaw, H. F. The nature and origin of authigenic smectites in some recent marine sediments. *Clay Minerals* 18, 239–252, doi:10.1180/claymin.1983.018.3.02 (1983).
49. Galán, E. in *Developments in Clay Science* Vol. 1 (eds Faïza Bergaya, Benny K. G. Theng, & Gerhard Lagaly) 1129–1162 (Elsevier, 2006).

50. Zhao, L., Dong, H., Edelmann, R. E., Zeng, Q. & Agrawal, A. Coupling of Fe(II) oxidation in illite with nitrate reduction and its role in clay mineral transformation. *Geochimica et Cosmochimica Acta* 200, 353–366, doi:https://doi.org/10.1016/j.gca.2017.01.004 (2017).
51. Kim, J. *et al.* Naturally occurring, microbially induced smectite-to-illite reaction. *Geology* 47, 535–539, doi:10.1130/G46122.1 (2019).
52. Robert, M. The Experimental Transformation of Mica Toward Smectite; Relative Importance of Total Charge and Tetrahedral Substitution. *Clays and Clay Minerals* 21, 167–174, doi:10.1346/CCMN.1973.0210305 (1973).
53. Canfield, D. E. Reactive iron in marine sediments. *Geochimica et Cosmochimica Acta* 53, 619–632, doi:https://doi.org/10.1016/0016-7037(89)90005-7 (1989).
54. Kostka, J. E. & Luther, G. W. Seasonal cycling of Fe in saltmarsh sediments. *Biogeochemistry* 29, 159–181, doi:10.1007/BF00000230 (1995).
55. Lueder, U. *et al.* Influence of Physical Perturbation on Fe(II) Supply in Coastal Marine Sediments. *Environmental Science & Technology* 54, 3209–3218, doi:10.1021/acs.est.9b06278 (2020).
56. Mackenzie Fred, T. & Kump Lee, R. Reverse Weathering, Clay Mineral Formation, and Oceanic Element Cycles. *Science* 270, 586–586, doi:10.1126/science.270.5236.586 (1995).
57. Rahman, S. in *Encyclopedia of Ocean Sciences (Third Edition)* (eds J. Kirk Cochran, Henry J. Bokuniewicz, & Patricia L. Yager) 216–227 (Academic Press, 2019).
58. Pickering, R. A. *et al.* Using Stable Isotopes to Disentangle Marine Sedimentary Signals in Reactive Silicon Pools. *Geophysical Research Letters* 47, e2020GL087877, doi:https://doi.org/10.1029/2020GL087877 (2020).
59. Mackin, J. E. & Aller, R. C. Diagenesis of dissolved aluminum in organic-rich estuarine sediments. *Geochimica et Cosmochimica Acta* 48, 299–313, doi:https://doi.org/10.1016/0016-7037(84)90252-7 (1984).
60. Mackin, J. E. CONTROL OF DISSOLVED AL DISTRIBUTIONS IN MARINE-SEDIMENTS BY CLAY RECONSTITUTION REACTIONS - EXPERIMENTAL-EVIDENCE LEADING TO A UNIFIED THEORY. *Geochimica Et Cosmochimica Acta* 50, 207–214, doi:10.1016/0016-7037(86)90170-5 (1986).
61. Mackin, J. E. & Aller, R. C. DISSOLVED AL IN SEDIMENTS AND WATERS OF THE EAST CHINA SEA - IMPLICATIONS FOR AUTHIGENIC MINERAL FORMATION. *Geochimica Et Cosmochimica Acta* 48, 281–297, doi:10.1016/0016-7037(84)90251-5 (1984).
62. Wang, C. *et al.* Early diagenetic alterations of biogenic and reactive silica in the surface sediment of the Yangtze Estuary. *Continental Shelf Research* 99, 1–11, doi:https://doi.org/10.1016/j.csr.2015.03.003 (2015).
63. Foteinis, S., Campbell, J. S. & Renforth, P. Life Cycle Assessment of Coastal Enhanced Weathering for Carbon Dioxide Removal from Air. *Environmental Science & Technology* 57, 6169–6178, doi:10.1021/acs.est.2c08633 (2023).
64. Saad, E. M. *et al.* Effect of cleaning methods on the dissolution of diatom frustules. *Marine Chemistry* 224, 103826, doi:https://doi.org/10.1016/j.marchem.2020.103826 (2020).

65. Kester, D. R., Duedall, I. W., Connors, D. N. & Pytkowic.Rm. PREPARATION OF ARTIFICIAL SEAWATER. *Limnology and Oceanography* 12, 176-& (1967).
66. Beckler, J. S., Kiriazis, N., Rabouille, C., Stewart, F. J. & Taillefert, M. Importance of microbial iron reduction in deep sediments of river-dominated continental-margins. *Mar. Chem.* 178, 22–34, doi:10.1016/j.marchem.2015.12.003 (2016).
67. Aller, R. C., Blair, N. E., Xia, Q. & Rude, P. D. Remineralization rates, recycling, and storage of carbon in Amazon shelf sediments. *Continental Shelf Research* 16, 753–786, doi:https://doi.org/10.1016/0278-4343(95)00046-1 (1996).
68. Mkadam Kombo Mohamed, Y. T., ALI Vuai Said, Tokuyama Akira. Dissolved aluminum and silica release on the interaction of Okinawan subtropical red soil and seawater at different salinities: Experimental and field observations. *Geochemical Journal* 40, 333–343 (2006).
69. Stookey, L. L. Ferrozine—a new spectrophotometric reagent for iron. *Analytical Chemistry* 42, 779–781, doi:10.1021/ac60289a016 (1970).
70. Strickland, J. D. & Parsons, T. R. A practical handbook of seawater analysis. (1972).
71. Ravel, B. & Newville, M. ATHENA, ARTEMIS, HEPHAESTUS: data analysis for X-ray absorption spectroscopy using IFEFFIT. *J Synchrotron Radiat* 12, 537–541, doi:10.1107/s0909049505012719 (2005).

Figures

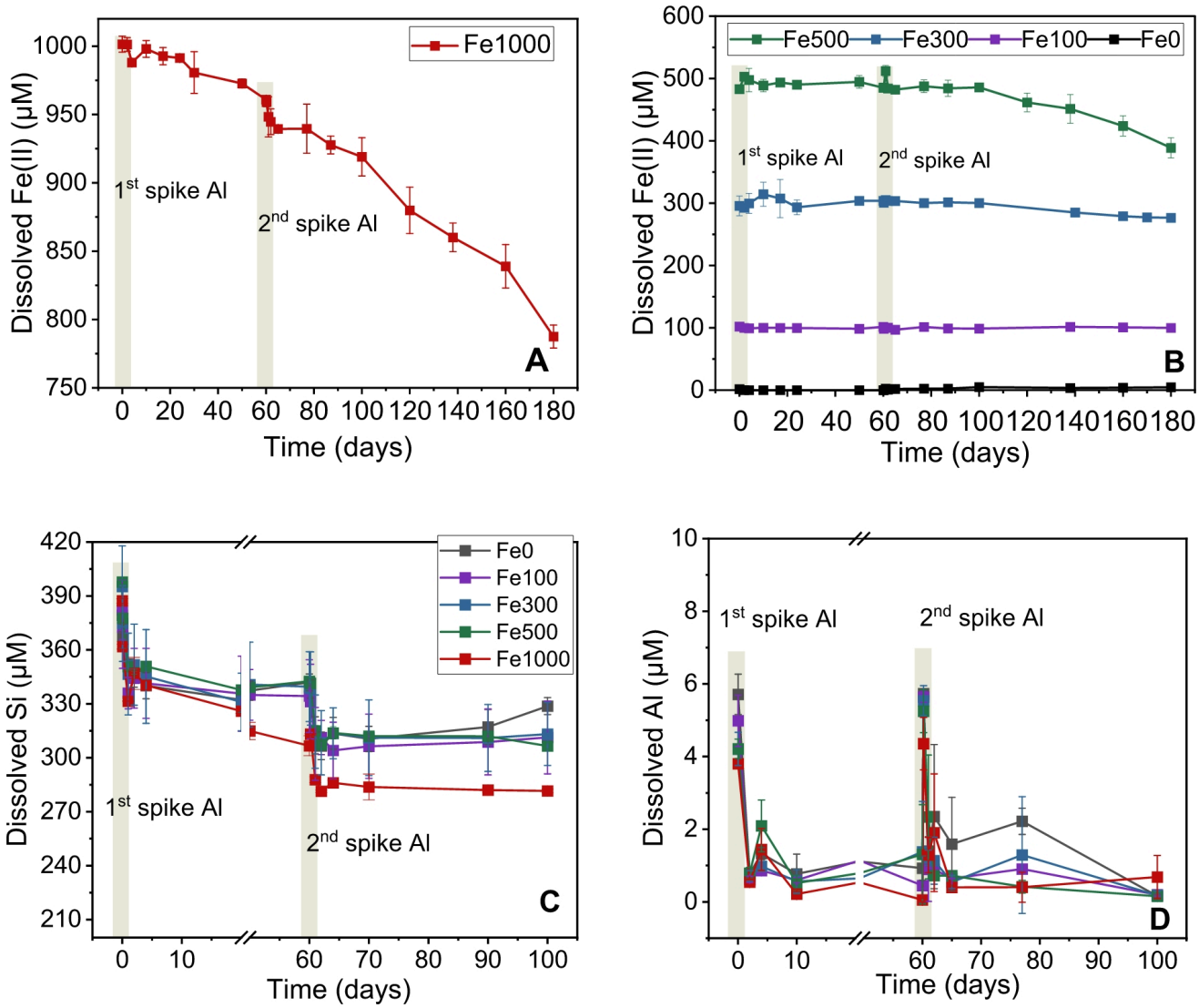


Figure 1

Evolution of solution phase: dissolved Fe^{2+} (A and B), Si (C), and Al (D) concentrations for treatments with 1000, 500, 300, 100, and 0 μM initial Fe^{2+} (Fe1000, Fe500, Fe300, Fe100, Fe0, respectively). (C) and (D) are the evolution of dissolved Si and Al concentrations, respectively. Error bars are standard deviation of replicate experimental groups

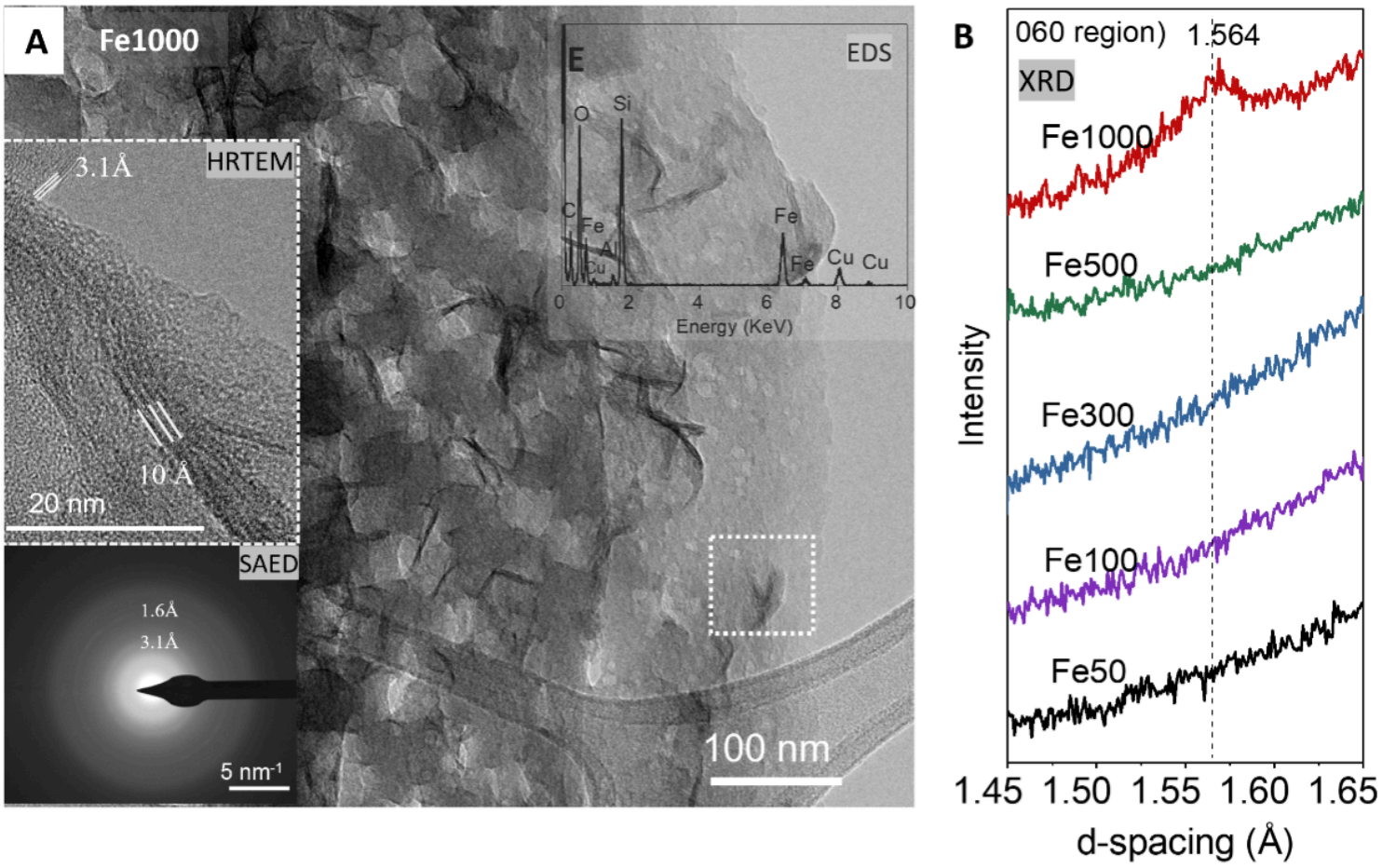


Figure 2

XRD and TEM analyses of reacted $bSiO_2$ phases after 60 days. (A) Synchrotron XRD patterns of all Fe^{2+} treatment groups, with new peak formation only identified in sample Fe1000. (B) TEM image showing the formation of fluffy phase on top of $bSiO_2$ in sample Fe1000. White dotted box indicates the location for HRTEM analysis in panel C. (C) HRTEM image showing d-spacings of 10 and 3.1 Å in the new phase with a turbostratic structure. (D) SAED of the new phase in C, showing a crystalline structure with d-spacings of 3.1 and 1.6 Å. (E) EDS showing a Fe-Mg-Al-Si chemical composition of the new phase.

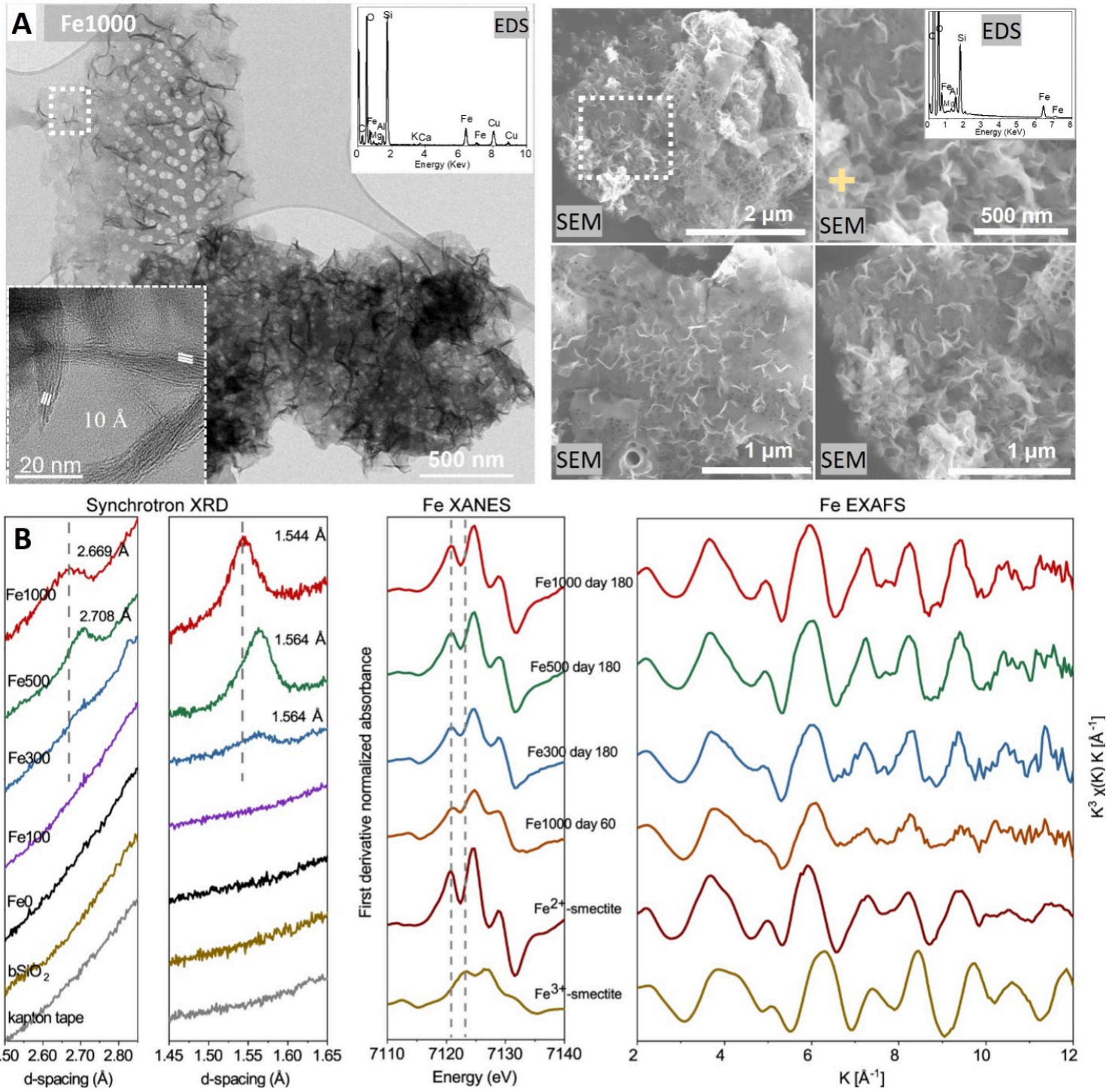


Figure 3

Formation of authigenic clay demonstrated by TEM and Synchrotron XRD and Fe K-edge XAS analyses after 180 days. (A) Fe1000 new phase TEM and SEM examination, (B) Synchrotron XRD and Fe K-edge XAS analyses of the reacted solids from Fe0 to Fe1000 treatments. (A) Aggregates of a flaky and curved new phase formed on $bSiO_2$ surface (showing $bSiO_2$ pores). A turbostratic layered structure and 10 Å d-spacing, typical of the smectite structure, were observed by HRTEM. SAED analysis of this new phase showed a smectite diffraction pattern and EDS analysis showed an Fe-Mg aluminosilicate composition. SEM analysis of multiple $bSiO_2$ particles show extensive growth of this new phase with a Fe-Mg

aluminosilicate composition. (B) Synchrotron XRD showed Formation of new peaks at 2.669 and 2.708 Å for Fe1000 and Fe500 treatments after 180 days, respectively. Fe XANES showed new peaks at 1.544 and 1.564 Å for Fe1000, Fe500, and Fe300 treatments. The first derivative of Fe K-edge XANES and Fe K-edge EXAFS confirm the formation of Fe^{2+}-smectites. Fe^{2+}-smectite spectra are from reference[39]. Fe^{3+}-smectite sample is a Fe^{3+}-dominated nontronite procured from the Clay Minerals Society.

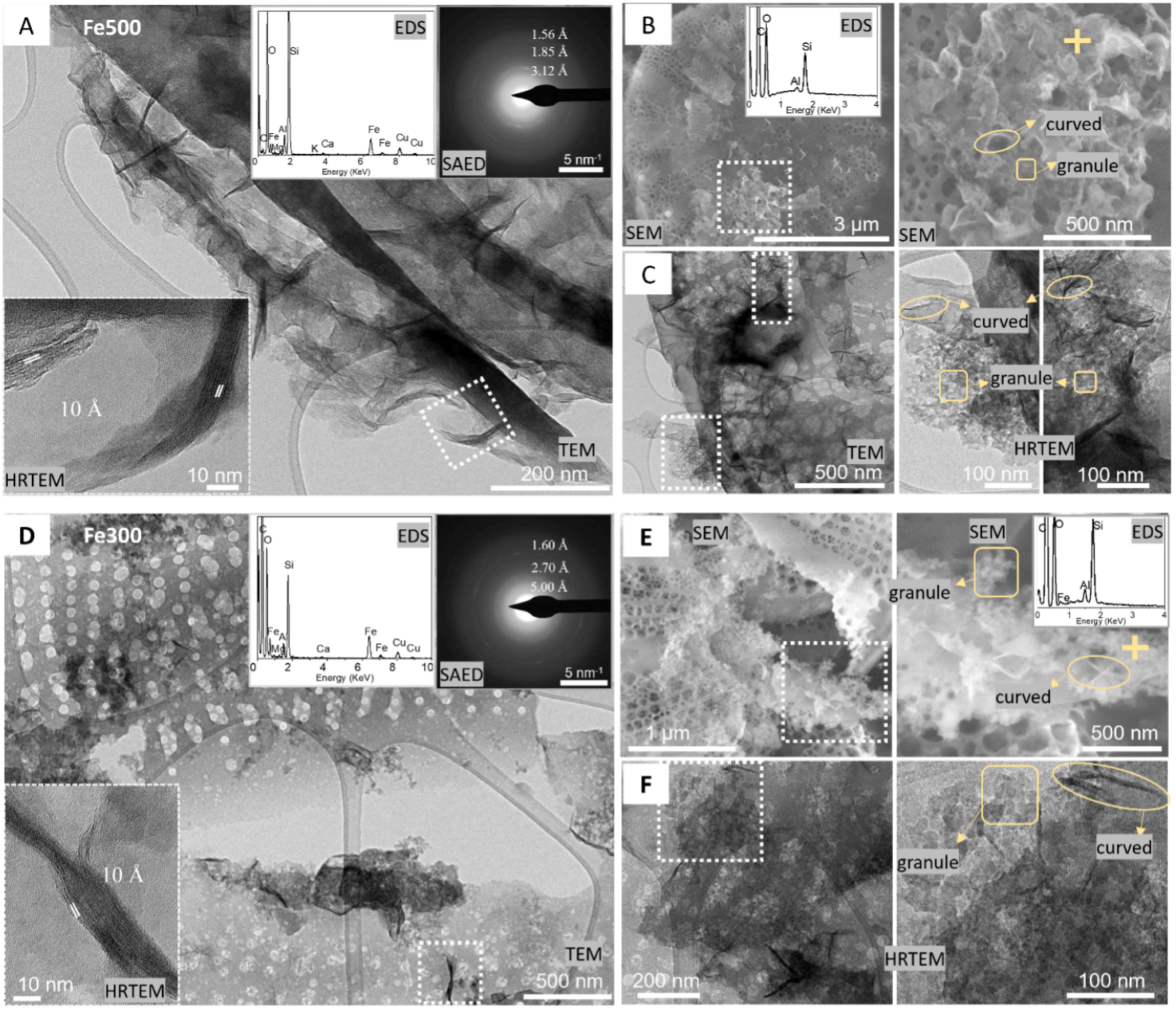


Figure 4

Examination of new authigenic phase formed after 180 days by TEM and SEM : Fe500 (A-C), and Fe300 treatments (D-F). A curved and flaky new phase was observed in the Fe500 treatment (A), showing a turbostratic layered structure with a 10 Å d-spacing under HRTEM. Smectite diffraction pattern and Fe-Mg aluminosilicate composition were also observed by SAED and EDS for this new phase. SEM analyses of multiple $bSiO_2$ particles show less extensive growth of the new smectite phase on $bSiO_2$

surface (B and C). A zoomed examination of the new phase showed a combination of less defined amorphous phase and the curved flaky phase. The amorphous phase showed a Si-Al composition by EDS. TEM and HRTEM analyses of the new phase further showed this Si-Al phase to be amorphous with no fringe lattice (referred to as amorphous granule phase as compared to the curved flaky Fe-smectite phase). The spatial association of the curved flaky phase and amorphous granule phase (B and C) suggest that the flaky phase grow out of the amorphous granule phase. In Fe300 treatment, a small amount of the curved flaky phase was observed (D), with a chemical composition and structure similar to the smectite observed Fe500 treatments. SEM and TEM analyses of multiple bSiO_2 particles show the dominance of the amorphous granule phase (E and F) with a Fe-Si-Al composition by EDS. The association of the curved flaky phase with the granule phase again indicates the flaky phase grew out of the granule amorphous phase.

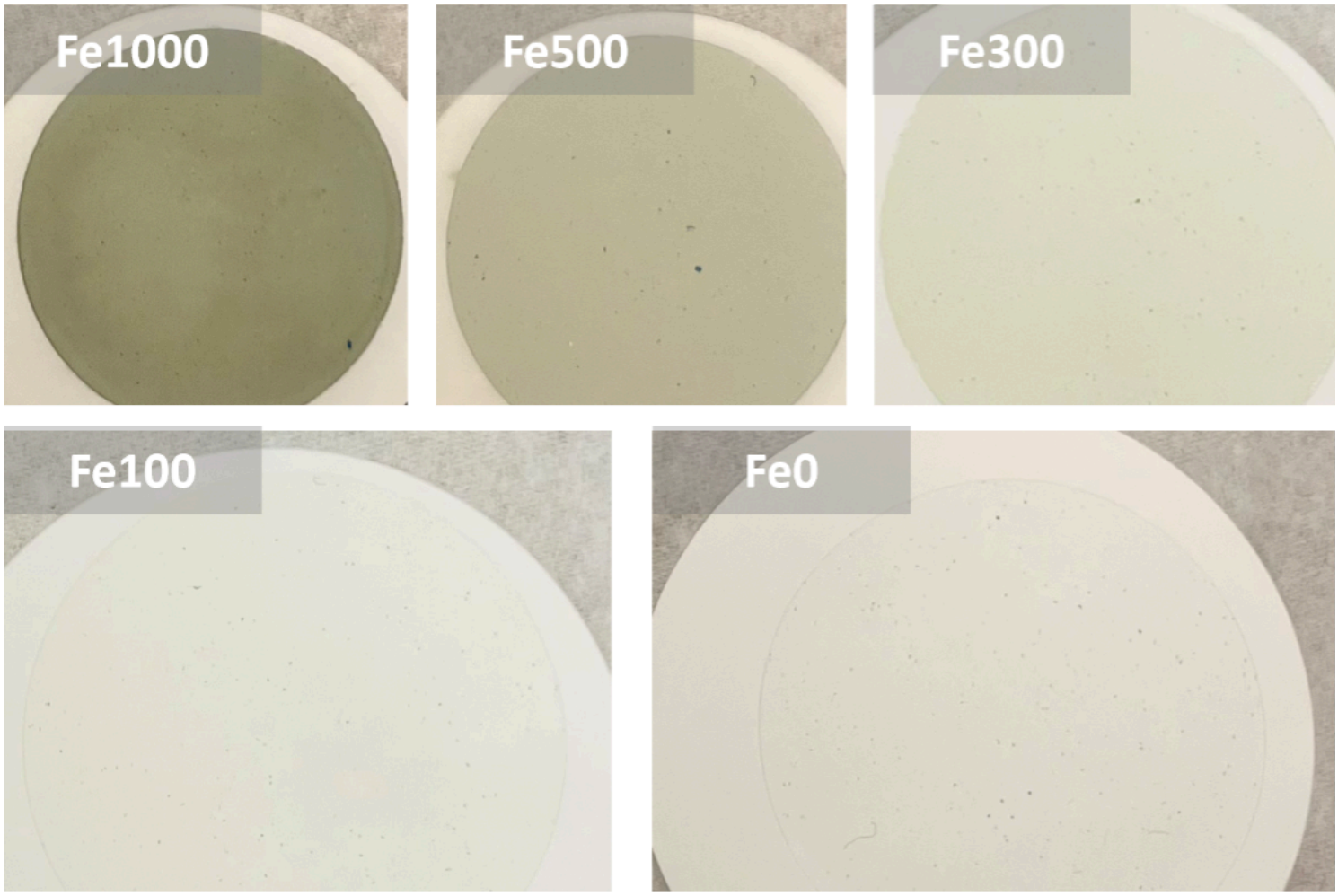


Figure 5

Green clay formation after 180 days of incubation. Harvested solids from the Fe1000, Fe500, and Fe300 treatments exhibited visible green coloration, whereas those from the Fe100 and Fe0 treatments did not.

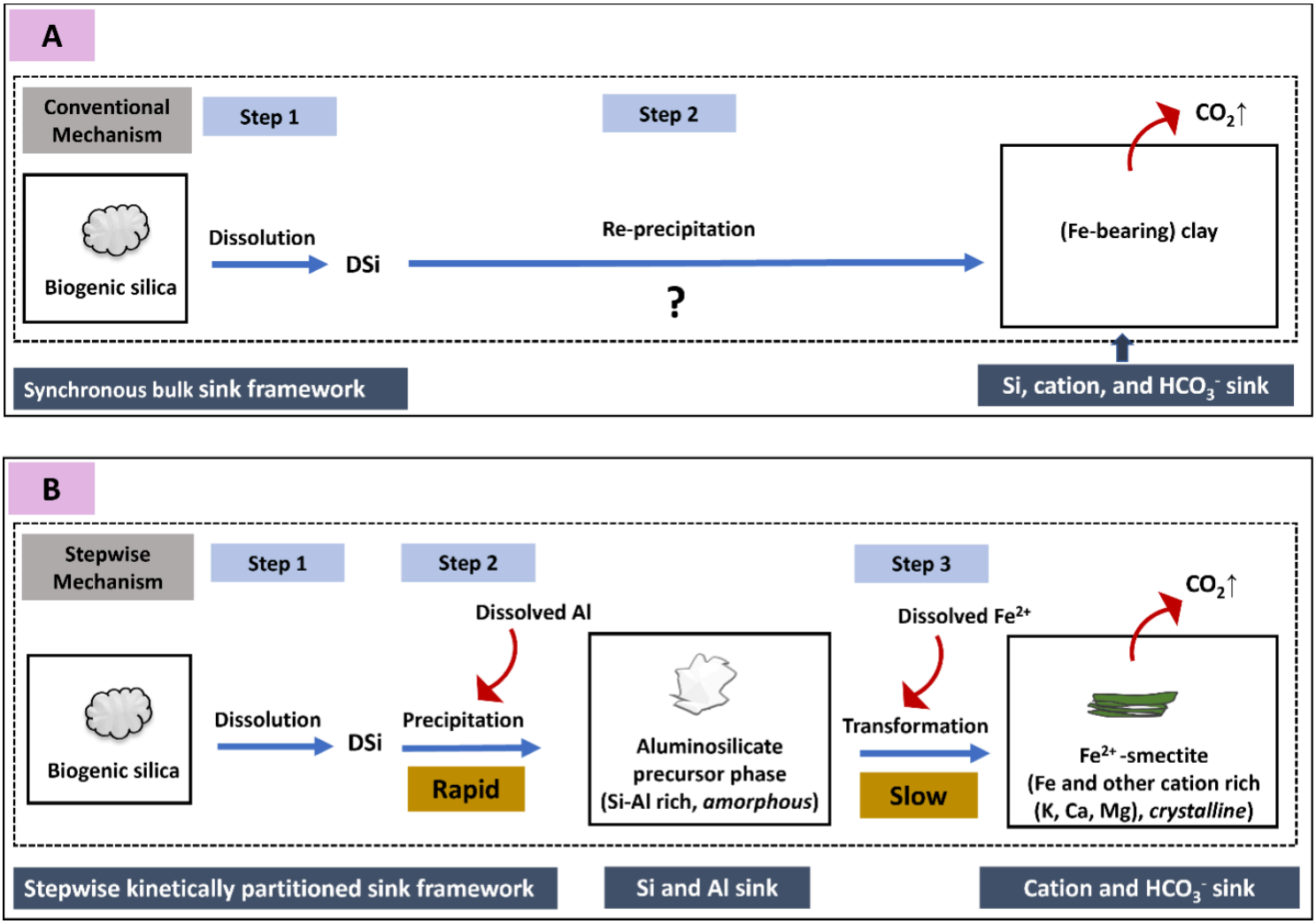


Figure 6

Schematic illustration of the conventional and updated elemental coupling in authigenic formation. (A) conventional synchronous equilibrium elemental partitioning model: intertwined Si, cation, and alkalinity sinks. (B) an updated stepwise model and associated stepwise elemental sinks: coupled Si and Al sink with decoupled cation and alkalinity sinks. Boxes represent starting, intermediate, and final phase(s). Red arrows denote elemental fluxes. DSi stands for dissolved Si.

Supplementary Files

This is a list of supplementary files associated with this preprint. Click to download.

- Zhaoetal.2026SI.docx